Chemical heterogeneity on Mercury's surface revealed by the MESSENGER X-Ray Spectrometer

Shoshana Z. Weider,[1] Larry R. Nittler,[1] Richard D. Starr,[2,3] Timothy J. McCoy,[4] Karen R. Stockstill-Cahill,[4] Paul K. Byrne,[1] Brett W. Denevi,[5] James W. Head,[6] and Sean C. Solomon[1,7]

Received 1 June 2012; revised 7 August 2012; accepted 14 August 2012; published 3 October 2012.

[1] We present the analysis of 205 spatially resolved measurements of the surface composition of Mercury from MESSENGER's X-Ray Spectrometer. The surface footprints of these measurements are categorized according to geological terrain. Northern smooth plains deposits and the plains interior to the Caloris basin differ compositionally from older terrain on Mercury. The older terrain generally has higher Mg/Si, S/Si, and Ca/Si ratios, and a lower Al/Si ratio than the smooth plains. Mercury's surface mineralogy is likely dominated by high-Mg mafic minerals (e.g., enstatite), plagioclase feldspar, and lesser amounts of Ca, Mg, and/or Fe sulfides (e.g., oldhamite). The compositional difference between the volcanic smooth plains and the older terrain reflects different abundances of these minerals and points to the crystallization of the smooth plains from a more chemically evolved magma source. High-degree partial melts of enstatite chondrite material provide a generally good compositional and mineralogical match for much of the surface of Mercury. An exception is Fe, for which the low surface abundance on Mercury is still higher than that of melts from enstatite chondrites and may indicate an exogenous contribution from meteoroid impacts.

Citation: Weider, S. Z., L. R. Nittler, R. D. Starr, T. J. McCoy, K. R. Stockstill-Cahill, P. K. Byrne, B. W. Denevi, J. W. Head, and S. C. Solomon (2012), Chemical heterogeneity on Mercury's surface revealed by the MESSENGER X-Ray Spectrometer, *J. Geophys. Res.*, *117*, E00L05, doi:10.1029/2012JE004153.

1. Introduction

[2] The MErcury Surface, Space ENvironment, GEochemistry, and Ranging (MESSENGER) spacecraft has been in orbit around the innermost planet since 18 March 2011. Early chemical remote sensing measurements made from orbit by MESSENGER's X-Ray Spectrometer (XRS) and Gamma-Ray Spectrometer (GRS) revealed that Mercury's surface is Mg-rich but Al- and Ca-poor compared with typical terrestrial and lunar crustal material, and that in terms of these elements the bulk surface is intermediate between low-Fe basaltic and komatiitic compositions [*Nittler et al.*, 2011]. Measured surface abundances of K [*Peplowski et al.*, 2011] and S [*Nittler et al.*, 2011] indicate that Mercury is not depleted in volatile elements relative to the other terrestrial planets, although this inference has been questioned [*McCubbin et al.*, 2012]. This chemical characterization places important constraints on the formation and early history of Mercury. Scenarios by which Mercury formed under highly reducing conditions, perhaps from material akin to the enstatite chondrites (albeit with higher density) [*Nittler et al.*, 2011], or from materials originally derived from comet-like anhydrous interplanetary dust particles that may also represent enstatite chondrite precursor material [*Ebel and Alexander*, 2011], have been proposed to account for the orbital observations.

[3] From Mariner 10 images, multiple geologic units were identified on the basis of their morphology and superposition relations, e.g., intercrater plains, heavily cratered terrain, and smooth plains (the last of which is characterized by flat to gently rolling plains, containing numerous wrinkle ridges and fewer impact craters than the intercrater plains) [*Trask and Guest*, 1975; *Spudis and Guest*, 1988]. From Mercury Dual Imaging System (MDIS) color data obtained during MESSENGER's first two Mercury flybys, *Denevi et al.*

[1]Department of Terrestrial Magnetism, Carnegie Institution of Washington, Washington, D. C., USA.
[2]Physics Department, Catholic University of America, Washington, D. C., USA.
[3]Solar System Exploration Division, NASA Goddard Space Flight Center, Greenbelt, Maryland, USA.
[4]Department of Mineral Sciences, National Museum of Natural History, Smithsonian Institution, Washington, D. C., USA.
[5]The Johns Hopkins University Applied Physics Laboratory, Laurel, Maryland, USA.
[6]Department of Geological Sciences, Brown University, Providence, Rhode Island, USA.
[7]Lamont-Doherty Earth Observatory, Columbia University, Palisades, New York, USA.

Corresponding author: S. Z. Weider, Department of Terrestrial Magnetism, Carnegie Institution of Washington, Washington, D. C. 20015, USA. (sweider@ciw.edu)

0148-0227/12/2012JE004153

[2009] mapped lateral heterogeneities in color and, by inference, surface crustal composition. Three units were distinguished on the basis of spectral slope, relative reflectance, and morphology: (i) smooth plains, (ii) intermediate terrain, and (iii) low-reflectance material. The smooth plains units tend to fill low-lying areas [*Denevi et al.*, 2009] and have lower densities of impact craters [*Strom et al.*, 2008]. Approximately 40% of Mercury's surface is covered by the smooth plains material [*Denevi et al.*, 2009], and although these deposits are widely distributed, two large expanses of smooth plains are associated with the Caloris impact basin [*Murchie et al.*, 2008] and the northern lowlands [*Head et al.*, 2011; *Zuber et al.*, 2012]. MESSENGER flyby and orbital data have confirmed the volcanic origin of most smooth plains units [*Robinson and Lucey*, 1997; *Head et al.*, 2008, 2011; *Murchie et al.*, 2008] and indicate that volcanism played a major role in the evolution of Mercury's crust [*Denevi et al.*, 2009].

[4] Although the first reports of orbital geochemical observations at Mercury largely concerned the global-scale surface composition of Mercury and its implications for planetary formation [*Nittler et al.*, 2011; *Peplowski et al.*, 2011], one XRS measurement presented by *Nittler et al.* [2011] provided ~100 km-scale resolution and suggested a difference in chemical composition between the northern smooth plains and the surrounding terrain. In this paper, we extend the analysis of MESSENGER XRS observations to a larger data set, one with sufficient spatial resolution to investigate regional-scale variations in surface composition in greater detail. A substantial proportion of the new XRS data reported here are from the northern smooth plains and the surrounding terrain, which is higher in crater density and therefore older than the smooth plains. We also include in the analysis a small amount of data from within, and adjacent to, the Caloris basin. Although Mariner 10 coverage does not include most of the region spanned by XRS data reported here, the terrain characteristics defined by *Trask and Guest* [1975] in their geological mapping allow us to classify the areas surrounding the northern smooth plains as a combination of intercrater plains and heavily cratered terrain (here abbreviated as IcP-HCT). In this paper we focus primarily on documented differences in chemical composition between the northern smooth plains units and the adjoining IcP-HCT. The results presented here complement the earlier work of *Nittler et al.* [2011].

2. MESSENGER X-Ray Spectrometer

[5] The abundances of major elements in the uppermost regolith (i.e., top ~100 μm) of planetary bodies in the inner solar system that do not possess an atmosphere can be measured through the technique of planetary X-ray fluorescence (XRF). When the flux of X-rays emitted from the solar corona is sufficient, atoms at the planet's surface are excited, and fluorescent X-rays, characteristic of the source atom, are emitted. The fluorescent X-rays can be detected by an orbiting XRS, and this information, combined with knowledge of the highly variable [e.g., *Donnelly*, 1976; *Bouwer*, 1983; *Crosby et al.*, 1993] incident solar X-ray spectrum (usually measured by an accompanying solar monitor), allows quantitative estimates of major rock-forming elemental abundance ratios in the surface material to be made. X-ray spectrometers have been included as part of the payloads on several missions to the Moon (e.g., Apollo 15 and 16 [*Adler et al.*, 1973], SMART-1 [*Grande et al.*, 2007; *Swinyard et al.*, 2009], SELENE [*Okada et al.*, 2002], and Chandrayaan-1 [*Narendranath et al.*, 2011; *Weider et al.*, 2012]); asteroids (NEAR-Shoemaker [*Trombka et al.*, 2000; *Nittler et al.*, 2001; *Foley et al.*, 2006; *Lim and Nittler*, 2009], and Hayabusa [*Okada et al.*, 2006]); and now Mercury with the MESSENGER X-Ray Spectrometer (XRS) [*Nittler et al.*, 2011] and the instrument in development for the future BepiColombo mission [*Fraser et al.*, 2010].

[6] The MESSENGER XRS consists of the Mercury X-ray Unit (MXU), which contains the three planet-facing gas-proportional counter (GPC) detectors, and the Solar Assembly for X-rays (SAX), which houses the solar-directed Si-PIN photodiode detector [*Schlemm et al.*, 2007]. All four detectors have an energy range of ~1–10 keV. Two of the GPC detectors have a thin foil placed in front of the detector: one of Mg, one of Al. The employment of this "balanced filter" [*Starr et al.*, 2000] approach enables signals from Mg, Al, and Si in the XRS spectra to be resolved. The detector resolution at higher energies is sufficient to separate the characteristic peaks of the heavier elements (e.g., S, Ca, Ti, and Fe).

[7] The XRS spectral accumulation period is varied with the location of MESSENGER along its highly eccentric orbit. When MESSENGER is close to periapsis, over the northern hemisphere, the XRS integration intervals shorten (to a minimum of 20 s); when the spacecraft is far from the planet the intervals increase (up to 450 s). Collimators on the GPC detectors give XRS a hexagon-shaped 12° field of view [*Schlemm et al.*, 2007], corresponding to a measurement "footprint" size on the surface ranging from <100 km in equivalent diameter at periapsis to >3000 km far from the planet. These dimensions are expressed in terms of the diameter of a circular footprint with the same area as the actual hexagon-shaped footprint, which is generally somewhat elongated along the ground track direction (though this effect is small; see Figure 3). The changing spacecraft altitude and instrument integration period therefore result in XRS measurements with varying spatial resolution on Mercury's surface, with the best spatial resolution at high northern latitudes.

[8] During typical solar conditions the incident X-ray flux to Mercury's surface is sufficient to induce fluorescence of elements up to an energy of ~2 keV (i.e., Mg, Al, and Si). During solar flares, the incident X-ray spectrum "hardens" and XRF from elements that fluoresce at higher energies occurs and can be detected. *Nittler et al.* [2011] presented results from solar-flare-induced XRF observations that were made almost exclusively when the spacecraft was in high-altitude portions of its orbit. Data presented in this paper were obtained during solar flares that occurred when MESSENGER was closer to periapsis. These measurements therefore have generally better spatial resolution on the surface of Mercury than those reported by *Nittler et al.* [2011].

3. Methodology

[9] In this work we analyzed XRF data from 16 solar flares that occurred prior to the end of 2011 (Table 1) and during which the MESSENGER spacecraft was at low

Table 1. Solar Flares Used for XRS Data Analysis

Date of Solar Flare	Number of Footprints	Total Integration Time (s)	Solar Temperature Range (10^6 K)
16 April 2011	4	200	8.9–12.2
22 April 2011	12	498	12.0–13.7
4 September 2011	6	240	11.0–16.0
6 September 2011	24	2040	11.0–13.6
13 September 2011	15	1013	11.4–15.5
15 September 2011	13	551	13.4–17.2
16 September 2011	16	960	11.1–16.4
19 September 2011	5	440	9.8–10.3
20 September 2011	9	564	9.1–11.1
25 September 2011	5	200	8.1–10.2
1 October 2011	12	473	10.0–11.1
2 October 2011	21	976	13.4–16.6
2 November 2011	38	758	10.3–17.2
3 November 2011	22	440	11.0–13.6
26 December 2011	11	220	9.6
27 December 2011	11	300	9.8–10.0

altitudes (all integration times are less than 100 s; the majority are 20 s or 40 s). The XRS GPC spectra chosen for this study contain analyzable signals within individual integration periods for elements with energies up to at least that of Ca (3.2 keV). We excluded any GPC spectra that show obvious fluorescence and bremsstrahlung contamination from energetic electron events, during which ~10–30 keV electrons interact with the XRS detectors and their constituent materials [*Ho et al.*, 2011, 2012; *Starr et al.*, 2012]. Exceptions to these selection criteria are the Caloris basin data. The individual GPC spectra for these two flares do exhibit Ca fluorescence, but at too low a level for reliable analysis. However, co-addition of spectra from several integrations provides sufficient signal to noise for Ca abundances to be determined for these flares. These spectra also show evidence for possible contamination by electrons, namely an elevated continuum at high energy suggestive of Cu fluorescence from the XRS collimators. Details of the analysis for the Caloris basin data are given in section 4.2. For all of the data, we used the forward modeling procedure of *Nittler et al.* [2011] to fit the incident solar and planetary XRF spectra and to generate elemental abundances for the regions observed, as described briefly in the following sections.

3.1. Fundamental Parameters

[10] An analytical fundamental parameters approach [e.g., *Clark and Trombka*, 1997; *Nittler et al.*, 2001] was employed to calculate theoretical fluorescence spectra, which were compared with the measured GPC spectra. In this calculation the fluorescence intensity of a given element in a spectrum depends on several factors: the shape and magnitude of the incident spectrum, the viewing geometry with which the observation is made, atomic physics parameters, and the concentrations of all constituent elements in the target. The XRS GPC spectra contain a contribution from scattered solar X-rays in addition to the fluorescent X-rays from Mercury's surface. These scattered X-rays must also be treated in the modeling in order to provide accurate abundance estimates. We use a theoretical formulation that incorporates the measurement viewing geometry and was derived from that of *Clark and Trombka* [1997] to determine the intensity of coherently scattered X-rays.

3.2. Solar Spectrum

[11] The forward modeling of the fluorescent and scattered X-rays requires knowledge of the incident solar X-ray spectrum, which is composed of many narrow lines, each a few eV in width. The relatively low-resolution SAX spectrum acquired for each observation was modeled in order to generate an equivalent high-resolution spectrum, using the theoretical *CHIANTI* code [*Dere et al.*, 1997]. The SAX spectrum modeling procedure involves: (i) fitting the low-energy electronic background to a power law of the form: background = $k \cdot \text{channel}^{-x}$, where k is a fitting parameter and the index x is derived from quiet solar conditions on the day of the observation; and (ii) fitting the spectrum by the variation of parameters that include the temperature of the plasma, the coronal abundances of elements with a low first ionization potential (as a group), and the coronal abundances of S, Ca, and Fe separately. Previous studies have indicated strong flare-to-flare variability in coronal elemental abundances [e.g., *Fludra and Schmelz*, 1999], which affects the shape of the observed SAX spectra. Figure 1 displays three example solar spectra and their derived fits at a variety of temperatures. Our solar modeling approach is based on the assumption that the emitting plasma is isothermal, but it has been shown [*Garcia*, 1994] that the plasma during the pre-peak period of a solar flare can have a multithermal nature. For this reason, following the practice used by *Nittler et al.* [2011], only integrations of XRF signals after the temperature peak of a solar flare are included in the subsequent elemental abundance analysis.

3.3. Detector Background

[12] Interactions between galactic cosmic rays or solar energetic particles with the GPC detectors create a spectral background that must be removed prior to elemental abundance modeling. This background tends to remain constant in shape on a tens of hours timescale, but it varies in magnitude, particularly when MESSENGER is close to periapsis and Mercury blocks a substantial portion of the cosmic ray flux. Here we derived background spectra by summing all the GPC spectra from the (Earth) day of the solar flare observation being analyzed for which the instrument FOV did not intersect with any portion of the sunlit planet ("dark spectra"). The shape of this background (for each of the detectors) was then scaled, as part of the fitting procedure (see below), to the GPC XRF spectrum that was being modeled.

3.4. GPC Spectral Fitting

[13] We employed a nonlinear χ^2 minimization routine, in which theoretical GPC spectra were repeatedly generated with varying parameters and compared with the measured spectrum until a best fit was obtained. Fixed modeling parameters included: (i) the high-resolution incident solar spectrum derived from SAX data (see section 3.2); and (ii) the viewing geometry (incidence, emission, and phase angles) for the observation. Fitting parameters included:

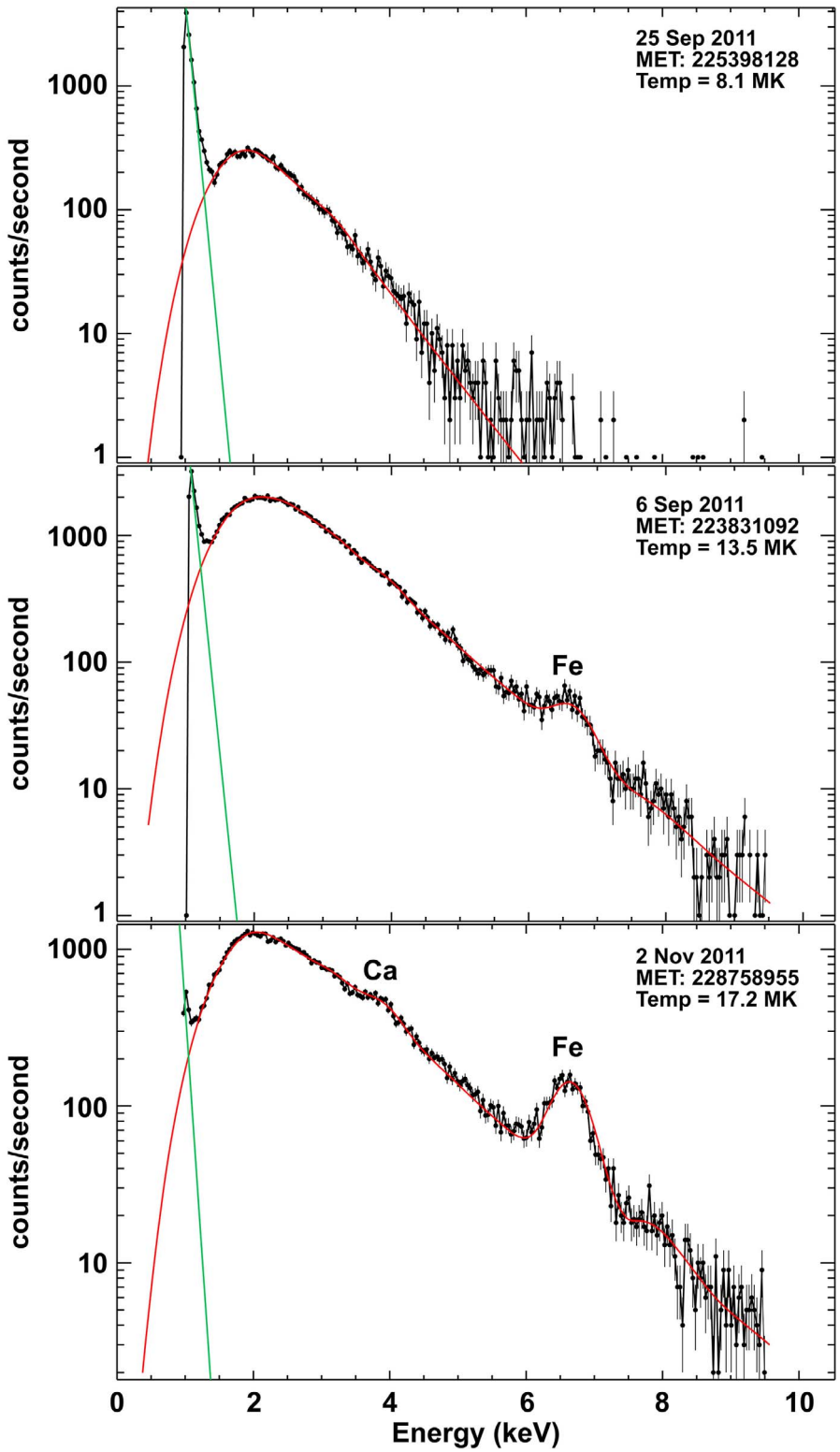

Figure 1. Three examples of fits to solar flare X-ray spectra measured by the SAX. The steeply inclined green line depicts the electronic background in the detector; the red line is the best fit solar spectrum (for the plasma temperature given in each case) convolved with the instrument response. The Ca and Fe line complexes (at ~3.6 keV and ~6.4 keV, respectively) increase in magnitude with temperature. MET = mission elapsed time, in s.

(i) elemental abundances (wt %) of Mg, Al, S, and Ca, as well as of Ti, Cr, Mn, and Fe for the largest flares; (ii) the energy calibration (the gain and energy of the zero channel) for and resolution of the detectors; and (iii) the magnitude of the detector background (see section 3.3). The relative abundance of Si was held fixed in the procedure, in order to ensure convergence of the fit. For each set of selected elemental abundances, an oxygen abundance, which cannot be measured by XRS, was assigned by the algorithm on the basis of typical reduced oxide stoichiometry. All elements were subsequently renormalized so that the sum of the weight percentages of the elemental oxides equaled 100%. The assumption of relatively constant Si is justified because of the small range of Si content in typical surface materials on the terrestrial planets, including Mercury [*Peplowski et al.*, 2012]. For the majority of integrations analyzed here, the three individual GPC spectra were fit separately to derive Mg and Al abundances. These values were then fixed in the modeling of a summed (all three GPC spectra) spectrum in order to obtain S and Ca abundances, as their signals are much lower in the individual GPC spectra. For some high-signal integration periods, all four elements could be modeled from the individual GPC spectra. The full elemental abundance modeling procedure was described by *Nittler et al.* [2011]. Figure 2 shows examples of fit summed XRF spectra for the three periods for which solar spectra are given in Figure 1.

[14] Systematic uncertainties arising from the background subtraction and solar spectrum modeling procedures, as well as from limitations to the fundamental parameters approach, were discussed in full by *Nittler et al.* [2011] and are larger (typically 5–10% for element/Si ratios) than the statistical errors we show here. Our elemental results do not display any correlations with solar flare temperature or viewing geometry. Any systematic uncertainties inherent to the modeling procedure are therefore unlikely to change the relative offsets between the different analyses. The compositional variability between different flares is much larger than that between integrations within a single flare (when gross differences in the geological units viewed are not involved) and thus the XRS data can be used to determine and map heterogeneities in elemental abundances.

[15] It is possible that individual spectra contain signals from the interactions of energetic electrons [*Ho et al.*, 2011, 2012] with the detectors. This is an additional source of systematic uncertainty that did not affect the data presented by *Nittler et al.* [2011]. Although we attempted to exclude such spectra, primarily through observations of strong fluorescence of Cu and/or Al from detector materials (the collimator and filter, respectively), it is possible that lower-level electron signals could go undetected and contribute fluorescent Mg and Al signals from the GPC filters to the analysis. The overall abundance of Al is relatively low on Mercury's surface, and so such background signals would have the largest effect on derived Al/Si ratios, which would thus be overestimated during energetic electron events. Energetic electrons are detected only when MESSENGER is close to the planet [*Ho et al.*, 2012]. The spectra analyzed by *Nittler et al.* [2011] were mainly acquired at large distances from the planet and thus were not susceptible to electron-induced spectral contamination. The range in the elemental ratios derived here (see section 4) and those reported by *Nittler et al.* [2011] are in good agreement, indicating that electron-induced signals are generally not a major contributor to our data set. However, anomalously high Al/Si ratios for some individual spectra cannot be ruled out, as discussed for the Caloris basin data in section 4.2.

4. Results

[16] The 205 individual XRS measurements analyzed here (data are tabulated in the auxiliary material) can be split into five groups according to the geological terrain on which their corresponding footprints lie.[1] As illustrated in Figure 3, these footprints lie on (i) the northern smooth plains, (ii) the surrounding terrain and other samples of IcP-HCT, (iii) some combination of both, (iv) the interior smooth plains of the Caloris basin, or (v) a combination of the circum-Caloris smooth plains and IcP-HCT. The derived elemental abundances, expressed as elemental weight ratios with respect to Si, are displayed in Figure 4. Results are presented for the northern smooth plains and IcP-HCT in section 4.1 and for the vicinity of the Caloris basin in section 4.2.

4.1. Northern Plains and Surrounding Terrain

[17] Chemical differences between the northern plains and the older surrounding regions are clearly indicated in Figure 4. These differences are highlighted by the histograms in Figure 5 and by the statistics given in Table 2. The data indicate that the IcP-HCT have, on average, higher Mg/Si, S/Si, and Ca/Si ratios, and a lower Al/Si ratio, than the northern plains. These differences are most clear for Mg/Si and S/Si; the Al/Si and Ca/Si differences between the two terrains are smaller (see Table 2).

[18] There appear to be two clusters of data points for the older terrain (Figure 4a): one with an Mg/Si ratio of ~0.75 and an Al/Si ratio of ~0.15, and another with Mg/Si and Al/Si ratios of ~0.45 and ~0.3, respectively. This bimodality is also clear in the histogram of Figure 5a and is discussed further in section 5.2. The sampled regions on Mercury's surface span a large range in compositions, one that is much larger, for example, than the range for terrestrial mid-ocean ridge basalts (MORB). As was previously observed from a much smaller data set [*Nittler et al.*, 2011], many of the sampled compositions in the older terrain are more similar to those of terrestrial komatiites, at least in terms of Mg/Si, Al/Si, and Ca/Si, than to terrestrial basalts.

4.2. Caloris Basin

[19] No XRS spectra from Caloris basin were selected when the criteria outlined in section 3 were applied. However, spectra with XRF signal up to Ca were obtained by co-adding several consecutive integrations from two solar flares on successive days (26 and 27 December 2011) in order to achieve sufficient signal-to-noise ratios. We co-added 11 spectra from the flare on 26 December 2011 and 10 spectra from the flare on 27 December 2011 (see Table 1) to obtain two summed spectra that were fit using the procedure described in section 3. Solar monitor spectra were fit separately for each individual integration period, and a weighted fit of the resulting best fit spectra was used

[1] Auxiliary materials are available at ftp://ftp.agu.org/apend/journal/2012JE004153.

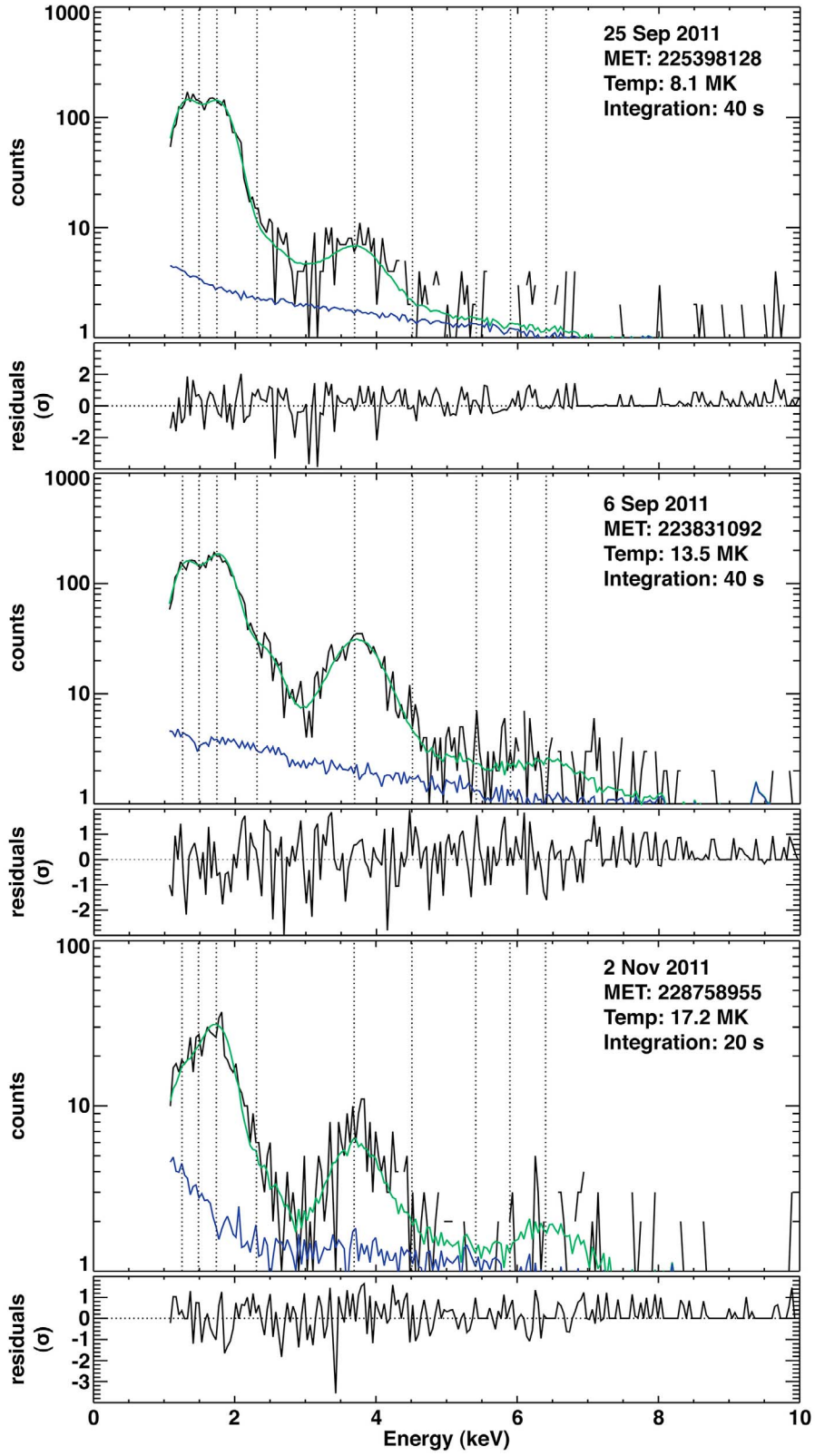

Figure 2. XRF spectra (black, primary signal) for the three time intervals for which solar spectra are shown in Figure 1. These spectra are the sum of the three separate GPC detector spectra. The best fit model (smooth curve) is shown in green, and the background level (lower signal) is shown in blue. Residuals between the best fit model and data are also shown in units of the counting-statistical error (σ) in each channel. Vertical dashed lines indicate the energy of K_α X-ray emission lines from (left to right) Mg, Al, Si, S, Ca, Ti, Cr, Mn, and Fe.

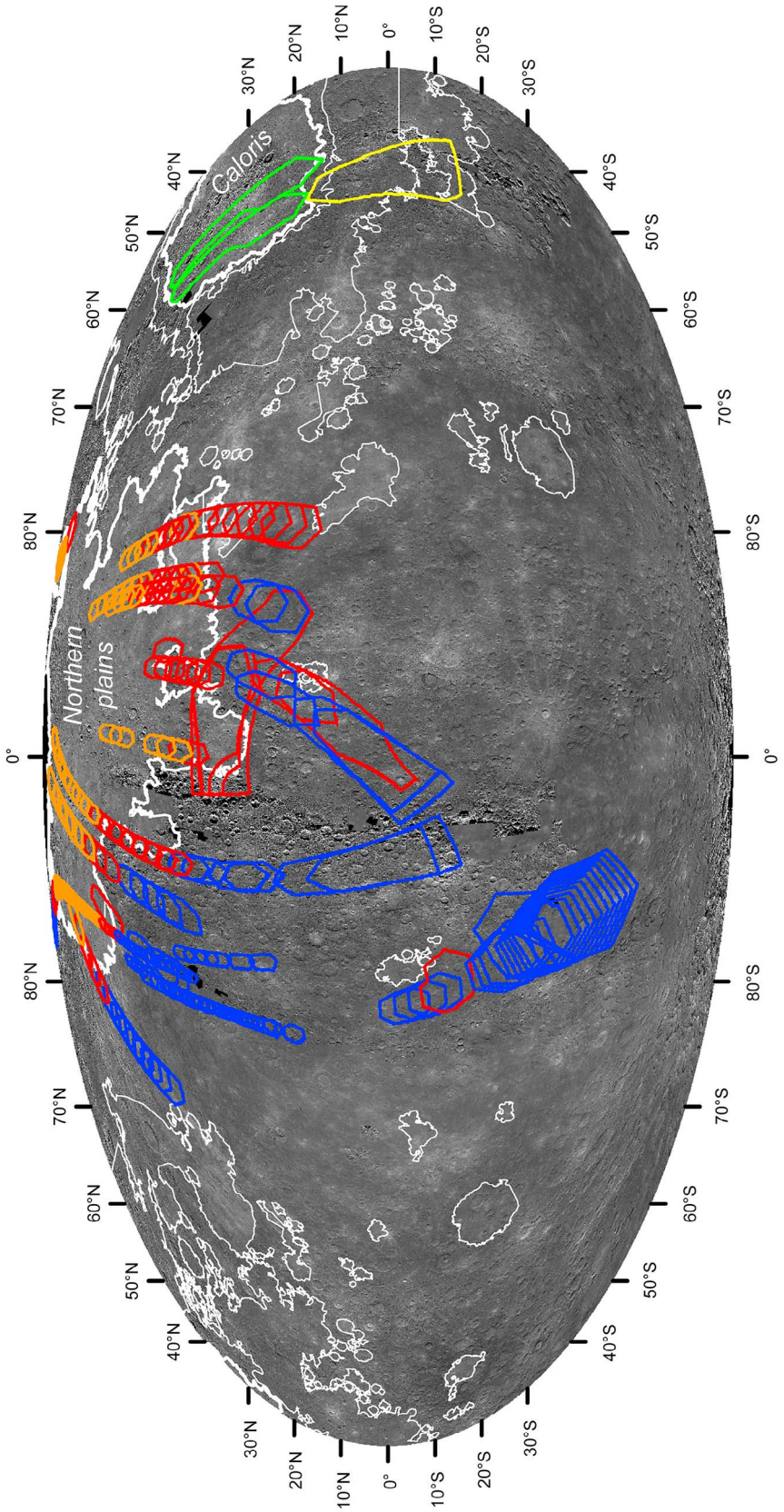

Figure 3. Footprints on Mercury of the 205 XRS observations from 16 solar flares analyzed here, projected onto the MDIS monochrome base map in Mollweide projection centered on 0° longitude [cf. *Becker et al.*, 2012]. Individual footprints are colored according to the terrain on which they lie (blue: intercrater plains and heavily cratered terrain (IcP-HCT); orange: northern smooth plains; red: mix of intercrater plains and heavily cratered terrain and smooth plains. Footprints associated with Caloris basin are also shown: green, Caloris interior smooth plains; yellow, mix of intercrater plains and heavily cratered terrain and circum-Caloris plains. White outlines show the boundaries of smooth plains units, mapped according to their morphology and superposed crater density [*Denevi et al.*, 2012].

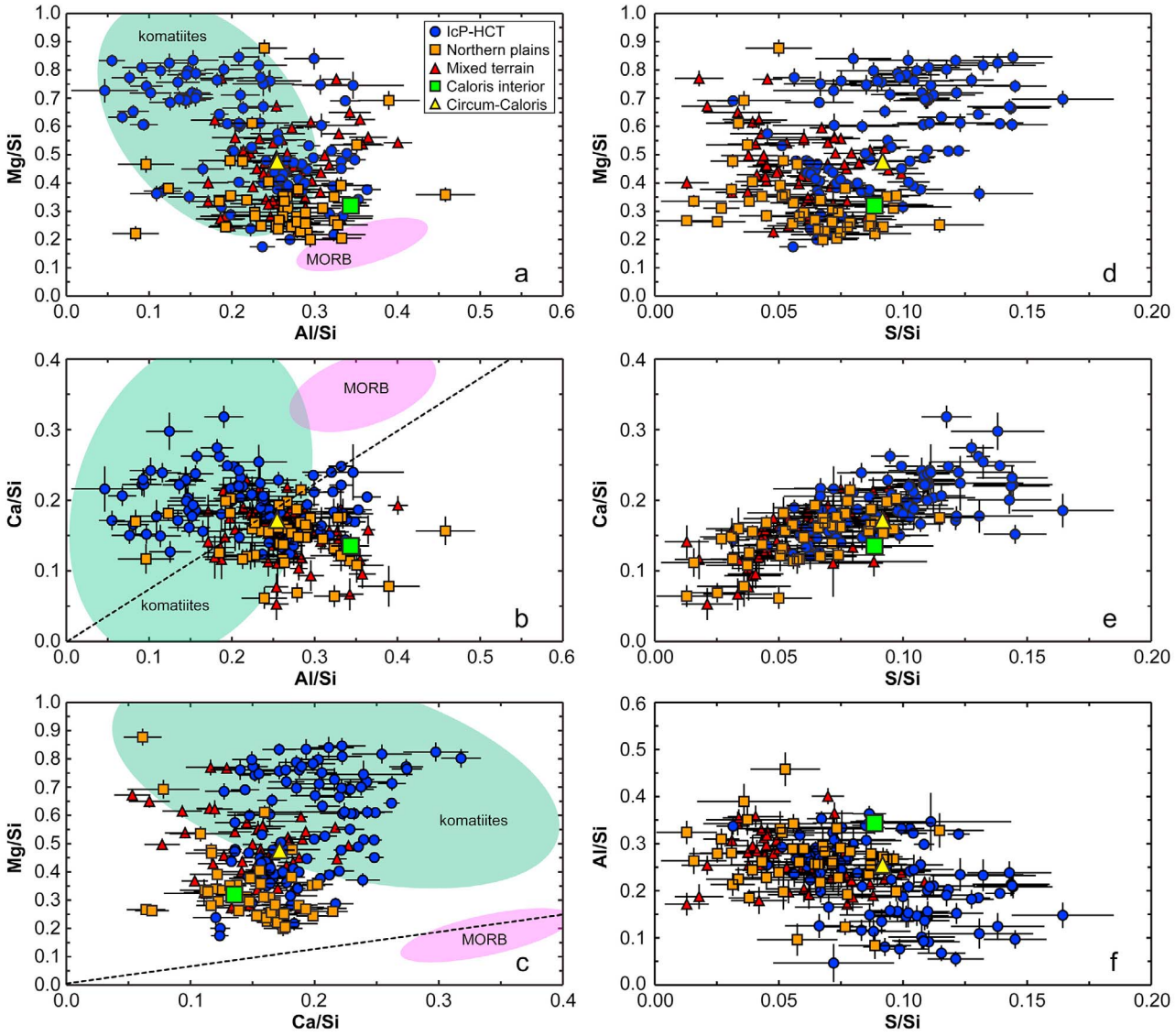

Figure 4. Elemental weight ratios inferred for the 205 analyzed footprints shown in Figure 3. (a) Mg/Si versus Al/Si; (b) Ca/Si versus Al/Si; (c) Mg/Si versus Ca/Si; (d) Mg/Si versus S/Si; (e) Ca/Si versus S/Si; and (f) Al/Si versus S/Si. The data are grouped according to the terrain on which the XRS footprint lies (blue circles: intercrater plains and heavily cratered terrain (IcP-HCT); orange squares: northern plains; red triangles: mix of IcP-HCT and smooth plains; green square: Caloris interior smooth plains; yellow triangle: mix of IcP-HCT and circum-Caloris smooth plains). Also shown in Figures 4a–4c are fields for the compositions of terrestrial komatiites (Geochemical Rock Database, http://georoc.mpch-mainz.gwdg.de/georoc/Entry.html) and mid-ocean ridge basalts (MORB) [*Jenner and O'Neill*, 2012]. The dashed lines in Figures 4b and 4c denote mixing lines between pure anorthite ($CaAl_2Si_2O_8$) with a Ca-, Al-free composition, and between pure diopside ($CaMgSi_2O_6$) with an Mg-, Ca-free composition, respectively.

as input to the fluorescence and scattering calculations. This use of an average solar spectrum may introduce some additional error to the analysis of the co-added XRS spectra, but any such error is expected to be small.

[20] The spectra from these two solar flares appear to contain contamination from electron events (i.e., there is Cu fluorescence evident in many of the integrations), and we therefore modeled the detector background differently from the procedure used for the rest of our data set (see section 3.3). Rather than using dark spectra to define the GPC backgrounds, the shape of the background signals for these spectra was determined by summing all the GPC spectra obtained from events with obvious electron-induced signals during December 2011. The magnitude of each GPC background was kept as a free parameter for the GPC fitting. The main effect of this non-standard background removal for the Caloris spectra was to yield Al/Si ratios about ~80% of those generated from spectra that were treated in the standard manner. Undetected electron contamination may therefore lead to a ~20% overestimate of Al/Si ratios for XRS spectra obtained close to Mercury, but as

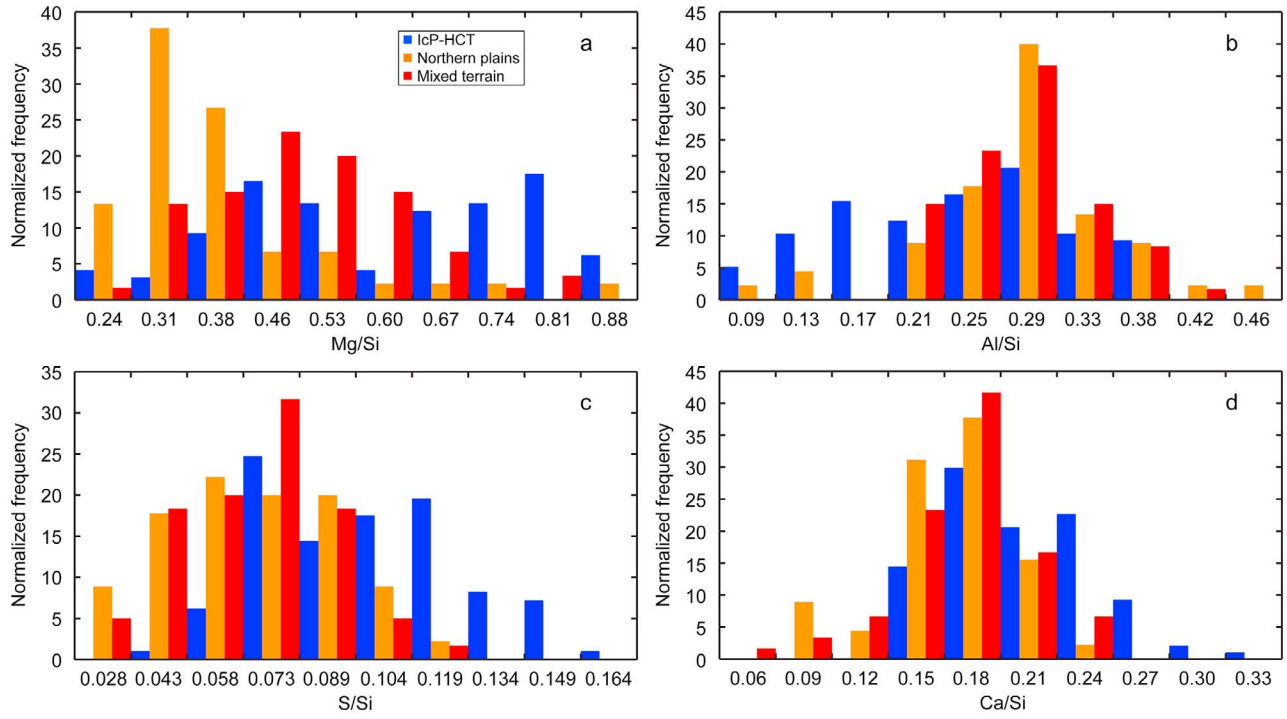

Figure 5. Histograms of elemental ratios for three footprint populations of XRS analyses by terrain type (excluding areas within or near the Caloris basin). (a) Mg/Si, (b) Al/Si, (c) S/Si, and (d) Ca/Si. The data are split into 10 equal size bins for each elemental ratio and are normalized to the total number of data points in the group; the bin upper limits are labeled on the abscissae.

discussed earlier such a bias is unlikely to have affected the majority of our data.

[21] The footprints of the 26 and 27 December summed spectra lie within the Caloris basin [*Fassett et al.*, 2009] (Figure 3) and its interior smooth plains deposits [cf. *Murchie et al.*, 2008]. The means of the elemental ratio values derived from these summed spectra from the two flares are shown in Figure 4. A separate integration from the 27 December 2011 flare has a footprint outside Caloris basin in an area consisting of a mixture of circum-Caloris smooth plains deposits and IcP-HCT. The GPC spectra for this integration were also modeled, and the derived elemental ratios are shown in Figure 4. The Caloris interior smooth plains have a composition that is consistent with that for the northern smooth plains deposits. The mixture of circum-Caloris plains and IcP-HCT is different from the interior smooth plains and is more similar to the other mixed terrains, insofar as having higher Mg/Si, Ca/Si, and lower Al/Si ratios.

5. Discussion

5.1. Possible Mineralogy

[22] The high Mg/Si ratio that we report, together with the low reported Fe/Si ratio [*Nittler et al.*, 2011], indicates that Mg-rich silicate minerals, such as enstatite and forsterite, dominate Mercury's surface. The correlation between Ca/Si and S/Si (Figure 4e) is the best between any two of the elemental ratios and is consistent for both the northern plains and the surrounding older terrain. The slope of the line (~1) is close to that for oldhamite, (Ca,Mg,Fe)S (meteoritic oldhamite is close to the end-member CaS [*Brearley and Jones*, 1998], which has a Ca:S weight ratio of 1.25), and may therefore be evidence that both the northern plains material and the older terrain contain varying amounts of this sulfide mineral. From ground-based reflectance spectroscopy measurements, the presence of oldhamite on the surface of Mercury has previously been suggested [*Sprague et al.*, 1995]. Moreover, oldhamite is ubiquitously found in enstatite chondrites as an accessory phase [*Mason*, 1966; *Keil*, 1968; *Buseck and Holdsworth*, 1972; *Leitch and Smith*, 1982; *Rubin*, 1983; *El Goresy et al.*, 1988; *Brearley and Jones*, 1998], e.g., in chondrules and with metals and other sulfides in complex mineral assemblages [*El Goresy et al.*, 1988]. Aubrite meteorites (enstatite achondrites) also commonly contain oldhamite as a minor phase [*Mittlefehldt et al.*, 1998], although some clasts in certain aubrites contain abundant (~30%) oldhamite [*Kurat et al.*, 1992; *Wheelock et al.*, 1994; *McCoy*, 1998]. The occurrence of oldhamite within these meteorites indicates that this mineral is stable under

Table 2. Mean, Standard Deviation (SD), and Median Elemental Ratio Values for the Intercrater Plains and Heavily Cratered Terrain (IcP-HCT) and Northern Plains (NP) Data Populations[a]

	Mg/Si		Al/Si		S/Si		Ca/Si	
	IcP-HCT	NP	IcP-HCT	NP	IcP-HCT	NP	IcP-HCT	NP
Mean	0.57	0.34	0.22	0.26	0.09	0.06	0.19	0.15
SD	0.18	0.13	0.08	0.07	0.03	0.02	0.04	0.04
Median	0.60	0.31	0.23	0.26	0.09	0.06	0.19	0.16

[a]Raw data are given in the auxiliary material.

highly reducing conditions [*Ebel*, 2006]. The sulfide-rich winonaite meteorites formed at slightly higher oxygen fugacities than the enstatite chondrites and do not contain oldhamite, but they also have much higher Fe abundances than the surface of Mercury [*Benedix et al.*, 2005].

[23] Although a correlation between Mg/Si and S/Si was noted by *Nittler et al.* [2011] from the early XRS results, such a relationship is less evident in our data (Figure 4d). However, both the enstatite chondrites and the aubrites contain other sulfide phases (e.g., niningerite: MgS, and daubreelite: $FeCr_2S_4$), and it is therefore possible that Mercury's surface contains other sulfides in addition to oldhamite. Moreover, the observation that Al/Si is slightly anti-correlated with S/Si (Figure 4f) indicates that oldhamite cannot be solely responsible for the Ca–S correlation since its abundance should not affect the Al/Si ratio. It is more likely that the Ca–S correlation reflects both the variable presence of CaS and the mixing of different silicate mineralogies (i.e., varying amounts of enstatite, forsterite, and plagioclase feldspar).

[24] Although the majority of the S may be contained within Ca-bearing sulfide phases, the majority of the Ca on Mercury's surface is likely contained within plagioclase feldspar (K. R. Stockstill-Cahill, Magnesium-rich crustal compositions on Mercury: Implications for magmatism from petrologic modeling, submitted to *Journal of Geophysical Research*, 2012). Ca/Si and Al/Si ratios do not correlate in Figure 4b as they would if Ca-rich plagioclase (anorthite, $CaAl_2Si_2O_8$) were the only Ca- and Al-bearing phase on Mercury's surface. It is possible that at least some of the Ca on Mercury's surface is found in one or more non-aluminous, non-sulfide phases, such as diopside ($MgCaSi_2O_6$). Diopside has been inferred to be present by *Sprague et al.* [2002] at equatorial regions between 275° and 315°E from ground-based astronomical observations. Figure 4c hints at a possible correlation between Mg and Ca, at least for the IcP-HCT, which would be satisfied by a Ca-rich pyroxene. However, such a mineral would not account for the measured Al, particularly for the more Al-rich northern plains. Na-rich ($NaAlSi_3O_8$) or K-rich ($KAlSi_3O_8$) feldspar may therefore be present in the northern plains material; we explore these possibilities below.

[25] The X-ray K_α energy of Na (~1.0 keV) is below the detection capability of XRS, and so no information on its abundance is available from the XRS data set. However, a non-spatially resolved measurement of Na by MESSENGER's GRS provides an estimated Na/Si ratio of ~0.1 for Mercury's surface [*Evans et al.*, 2012]. This Na abundance would allow a substantial albite content and could account for a large proportion of the Al on Mercury's surface. It is also known that the abundances of neutral and ionized Na in Mercury's exosphere are spatially variable and enhanced at high latitudes [*McClintock et al.*, 2009; *Vervack et al.*, 2010; *Zurbuchen et al.*, 2011]. However, it remains uncertain how the exosphere distributions relate to the interplay between source processes and variations in surface composition [e.g., *Killen et al.*, 2001, 2004; *Mura et al.*, 2009]. We also note that albitic plagioclase constitutes up to ~16% of aubrites [*Watters and Prinz*, 1979].

[26] Although K can theoretically be detected by XRS as a low-energy shoulder on the Ca line if it is sufficiently abundant at the surface, only XRS spectra from the largest solar flares show any evidence for a K signal. The K abundance, however, remains difficult to quantify because of the possibility that Ca XRF causes secondary K fluorescence (i.e., fluorescent Ca X-rays may induce some fluorescence of K in addition to that caused by incident solar X-rays because of the proximity of the Ca K_α emission energy, 3.69 keV, to the K K-edge absorption energy, 3.61 keV). *Peplowski et al.* [2012] reported spatial variations in the surface abundance of K in Mercury's northern hemisphere and, in particular, showed that an area approximately, but not precisely, corresponding to the northern plains contains more K (~2000 ppm) than the surrounding terrain (~500 ppm). Although this variation provides further evidence for the compositional differences between terrain types reported here, the low abundance of K is insufficient to account entirely for the Al-bearing phase(s) on Mercury's surface, which are likely to be dominated by Ca- and Na-bearing feldspars. It should also be noted that *Peplowski et al.* [2012] did not find the Caloris basin to be a region of high K abundance. *Peplowski et al.* [2012] hypothesized that the observed variation in the abundance of K across Mercury's northern hemisphere is dominantly the result of a surface heating process that mobilizes and redistributes K from equatorial and hot-pole regions to the exosphere and/or the polar regions. If K is more susceptible to these thermal mobilization processes than the elements measured by XRS, then the compositional similarity between the northern plains and Caloris interior smooth plains units as observed by XRS together with the differences in K abundance measured by GRS lends credence to their hypothesis.

[27] Stockstill-Cahill et al. (submitted manuscript, 2012) utilized the MELTS program [*Ghiorso and Sack*, 1995; *Asimov and Ghiorso*, 1998] to model the crystallization of candidate magmas on Mercury having compositions derived from XRS and GRS measurements of surface elemental abundances. They found that the surface of Mercury is most similar to terrestrial magnesian basalts (with MgO content adjusted to account for the low FeO on Mercury's surface) and is likely to be mineralogically dominated by Mg-rich orthopyroxene (enstatite) and plagioclase. High degrees of partial melting in the source regions are required to have produced such Mg-rich lavas; the derived melt would have erupted at high temperatures and with low viscosities. The MELTS modeling is not calibrated for the high S concentrations and low oxygen fugacity inferred to have existed during Mercury's early history. For this reason, S was removed (with Mg and Ca, according to the proportions reported by *Nittler et al.* [2011] and *McCoy et al.* [1999]) from the bulk compositions modeled in their work. Stockstill-Cahill et al. (submitted manuscript, 2012) suggested that Mercury's surface has a sulfide abundance of 2–3 wt%. Their modeling also indicated that Ca on Mercury's surface is mostly contained within anorthositic plagioclase feldspar, although this finding may change when similar calculations are conducted with the most recent Na abundance estimates from GRS.

5.2. Northern Plains Versus IcP-HCT

[28] Some of the geochemical differences between the northern plains and the surrounding IcP-HCT are summarized in Table 3. In terms of elemental abundances the two terrains appear to be distinct, with the northern plains regions characterized by lower abundances of Mg, Ca, and

Table 3. Summary of the Characteristics of the Northern Plains and Surrounding Intercrater Plains and Heavily Cratered Terrain (IcP-HCT)[a]

	Northern Plains	IcP-HCT
Age	3.7–3.8 Ga[b]	4.0–4.2 Ga[c]
Mg	~8.5 wt%	~14.4 wt%
Fe	Up to ~4 wt%[d]	Up to ~4 wt%[d]
Ca	~3.7 wt%	~4.9 wt%
S	~1.5 wt%	~2.3 wt%
Al	~6.6 wt%	~5.4 wt%
K	~2000 ppm[e]	~500 ppm[e]

[a]Approximate elemental abundances for Mg, Al, S, and Ca are calculated by multiplying the mean ratios (relative to Si) of the data presented in this paper by 25 wt% Si.
[b]The inferred age of the northern plains is taken from *Head et al.* [2011].
[c]The approximate age of the IcP-HCT is taken from *Strom and Neukum* [1988].
[d]The estimated Fe abundance is taken from *Nittler et al.* [2011].
[e]The K abundances are taken from *Peplowski et al.* [2012].

S, and higher Al and K. One possible explanation for the lower Mg/Si ratios in the northern plains is Fe substitution for Mg in mafic minerals. To account for the ~6 wt% difference in Mg between the two terrains, a substitution of ~2.5 wt% Fe (~3.2% FeO) into the mafic silicates in the northern plains is required. Even such an FeO content is consistent with the upper limits imposed by the absence of a 1 μm absorption band in reflectance spectra of Mercury's surface (~6 wt% FeO for mature material [*Vilas*, 1988; *Blewett et al.*, 2002], and ~3 wt% FeO for fresh material [*McClintock et al.*, 2008]). However, the higher albedo of the northern plains [*Denevi et al.*, 2009] compared with that for IcP-HCT does not suggest a higher Fe content. Fe abundance estimates from XRS data can be made only during the most energetic flares and from integrations sufficiently long to provide good signal-to-noise ratios in the GPC spectra. The short integration times involved in the acquisition of our high-spatial-resolution data make it difficult to estimate Fe abundances at the same resolution as for those elements with lower atomic numbers. To obtain Fe abundance estimates for a number of sites over the surface of Mercury, several consecutive integrations must be summed and then modeled.

[29] The bimodality of the compositional data noted in section 4 for the IcP-HCT suggests that the older crust on Mercury is heterogeneous. It appears that the older terrains consist of at least two distinct lithologies: (i) an ultramafic composition consisting mainly of enstatite with some plagioclase and oldhamite; and (ii) a more typical basalt with some sulfide content, i.e., a composition more similar to that of the northern plains material (see Figures 4a, 4c, and 4d). Determination of surface composition from solar flares that occur when MESSENGER is closer to apoapsis, as well as from more quiet-Sun data (for Mg/Si and Al/Si ratios), will help determine if this bimodality in composition applies globally, and if differences in composition correlate with geological units mapped on the basis of spectral reflectance, morphology, stratigraphy, or topography.

[30] The chemical differences between the northern plains and surrounding terrain provide possible insight into the evolution of Mercury's mantle. The lower Mg content of the northern plains suggests that this material derives from a source that was more evolved (i.e., Mg-depleted) and cooler than that which produced much of the older material in the IcP-HCT. This inference is consistent with the younger age of the northern plains [*Head et al.*, 2011] (Table 3). Partial remelting of a komatiitic source produces a MORB-like composition. If the northern plains were a product of remelting of the source region for the older IcP-HCT (more komatiitic on average), the trends between the two populations would be similar in direction to the komatiite-MORB trends in Figures 4 and 6. This pattern is not observed; therefore it is more likely that the lavas of the two terrains derived from different portions of Mercury's mantle. By this reasoning, earlier, higher degrees of partial melting yielded the high-temperature magmas that typically formed the IcP-HCT, and later melting of separate portions of the mantle, at lower temperatures and degrees of partial melting, produced the magmas that formed the northern plains (and the plains interior to the Caloris basin).

5.3. Possible Meteorite Analogues for Mercury

[31] It has been suggested [*Burbine et al.*, 2002; *Nittler et al.*, 2011] that Mercury accreted from precursor materials that were similar in composition to the enstatite chondrites, albeit with higher bulk Fe content to account for the planet's high density. An alternative hypothesis is that the enstatite chondrite parent body and Mercury may have accreted independently from material of similar composition [e.g., *Ebel and Alexander*, 2011]. Aubrites are thought [e.g., *Mittlefehldt et al.*, 1998] to be related to the enstatite chondrites as they share similar mineralogies [*Keil*, 1968; *Watters and Prinz*, 1979] and oxygen isotope compositions [*Clayton et al.*, 1984]. Aubrites consist mainly of enstatite and minor amounts of plagioclase, diopside, olivine, metallic Fe-Ni, and sulfides [*Watters and Prinz*, 1979]. They are interpreted as representing the residual silicates after the partial melting of a highly reduced source and removal of the basaltic material, and they have been proposed as a possible meteoritic analogue to Mercury's surface composition [*Burbine et al.*, 2002].

[32] The MgO–CaO–Al_2O_3 ternary plot in Figure 6 compares the compositional data for the northern plains and IcP-HCT with enstatite chondrite partial melt [*McCoy et al.*, 1999] and aubrite [*Watters and Prinz*, 1979] compositions. The high-temperature partial melts (representing high degrees of partial melting) of the enstatite chondrite Indarch provide a generally good match to our data. Figure 7a highlights additional similarities in elemental abundances (relative to CI chondrites) between the Indarch high-temperature partial melts and the surface composition of Mercury. The Mercury abundances generally fall within the range exhibited by the 1400°C and 1500°C partial melts, although the S content on Mercury's surface is lower than that within the melt compositions, and the poorly constrained surface Fe content appears to be considerably higher. The aubrite elemental abundances are not a close match to Mercury surface compositions. That the surface of Mercury is more similar to basaltic melt derived from an enstatite-chondrite-like source region than to the residual silicates such as the aubrites are thought to represent is consistent with the widespread presence on Mercury of volcanic plains [*Denevi et al.*, 2009]. *McCoy et al.* [1999] suggested that partial melting of enstatite chondrite material would produce broadly basaltic (enstatite–plagioclase) compositions, with substantial amounts of crystallized sulfides; their conclusion is in qualitative agreement with our findings (see section 5.1).

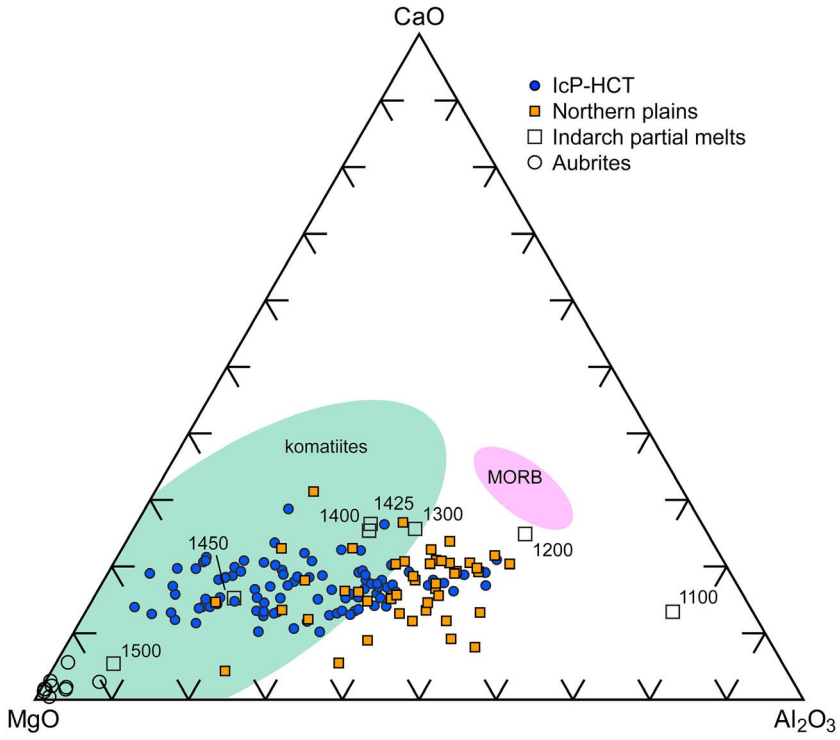

Figure 6. MgO-Al_2O_3-CaO ternary diagram showing the compositions of the areas of the northern plains and intercrater plains and heavily cratered terrain (IcP-HCT) viewed by XRS. These data have been converted from elemental ratios to oxide wt% values under the assumption that Si is at 25 wt% in all areas. Also shown are the (i) compositions of the products of seven partial melting experiments (squares, labeled with the maximum temperature in °C) with the enstatite chondrite Indarch [*McCoy et al.*, 1999], (ii) compositions of ten aubrite meteorites [*Watters and Prinz*, 1979] (circles), and (iii) fields of terrestrial komatiites (Geochemical Rock Database) and mid-ocean ridge basalts (MORB) [*Jenner and O'Neill*, 2012].

However, the use of partial melts of enstatite chondrites as compositional analogues for Mercury surface material does not account for the lower Fe abundances of the former. It is possible that the surface of Mercury contains almost no indigenous Fe and that much of what is present has been exogenously delivered by meteoroid impacts.

5.4. Mercury Compared with Earth and the Moon

[33] The early orbital XRS results [*Nittler et al.*, 2011] indicated important differences between the crustal composition of Mercury and those of Earth and the Moon. The findings that the surface of Mercury is richer in Mg and S, and poorer in Al, Ca, and Fe are corroborated by the work presented here, as highlighted in Figures 4, 6, and 7. The description of Mercury's surface as intermediate in composition between komatiites and typical basalts remains broadly applicable, at least in terms of Mg, Al, and Ca, although Stockstill-Cahill et al. [submitted manuscript, 2012] have suggested that a noritic composition (orthopyroxene and labradorite) may be a more appropriate description. In any case, it is clear that the high abundance of S and the low Fe content on Mercury's surface are unlike typical crustal rocks found on either Earth or the Moon.

6. Conclusions and Future Work

[34] The analysis and categorization of 205 spatially resolved XRS measurements have demonstrated that the major element composition of Mercury's northern smooth plains differs from that of the older surrounding terrain. The older terrain generally has higher Mg/Si, S/Si, and Ca/Si ratios, and a lower Al/Si ratio, than the northern plains. Mercury's surface mineralogy is dominated by high-Mg mafic (mostly enstatite) and plagioclase feldspar (calcic and sodic) phases, with smaller amounts of sulfide minerals (e.g., oldhamite). The smooth plains within the Caloris basin are similar in composition to the northern plains. The elemental abundance differences between these two large expanses of smooth plains and older terrain indicate that the lavas which formed the smooth plains were more chemically evolved and had different mantle sources than the magma from which Mercury's older areas of crust were derived. High-degree partial melts of enstatite chondrite material are a generally good compositional and mineralogical match, albeit with less iron, for much of the surface of Mercury.

[35] How the northern plains compare compositionally to the other smooth plains units that are globally distributed over the rest of Mercury's surface is a major question we can only begin to address. Answering this question will require the acquisition and analysis of additional, more globally distributed XRS spectra for which the footprints fall entirely within other smooth plains units. From the small amount of data analyzed for Caloris basin it appears that its interior smooth plains are similar in major-element composition to

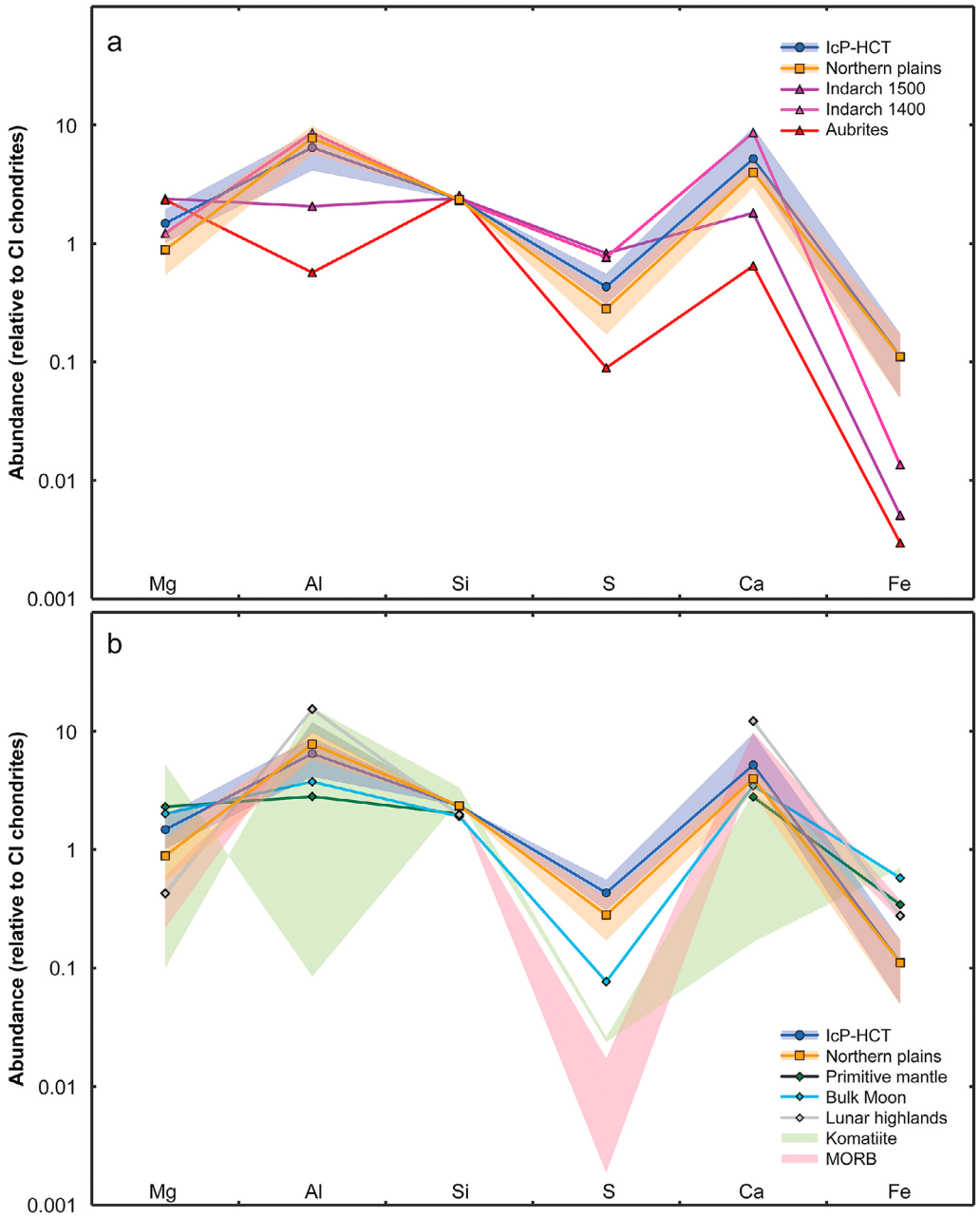

Figure 7. Mean abundances (relative to CI chondrites) of Mg, Al, Si, S, Ca, and Fe in the northern plains and intercrater plains and heavily cratered terrain (IcP-HCT) compared with (a) 1500° and 1400° partial melts of the Indarch enstatite chondrite [*McCoy et al.*, 1999] and a mean value for the aubrite meteorites [*Watters and Prinz*, 1979]; and (b) the primitive terrestrial mantle [*Palme and O'Neill*, 2003], the bulk Moon [*Anders*, 1977; *Taylor*, 1982], the lunar highlands [*Taylor*, 1982], komatiites (Geochemical Rock Database), and mid-ocean ridge basalts (MORB) [*Jenner and O'Neill*, 2012]. The fields for the northern plains and IcP-HCT represent one-standard deviation variations from the means of the individual footprint values. The Fe abundances for the Mercury compositions are derived from *Nittler et al.* [2011] and are taken to be identical for both terrain types. The komatiite and MORB fields indicate the variation between high- and low-Mg end-members of both groups. CI chondrite abundances are taken from *Palme and Beer* [1993] and *Palme and Jones* [2003].

the northern smooth plains, but more data are required to confirm this finding. Additional comparisons will enable a more complete view of Mercury's surface compositions and likely mantle sources. Additional petrologic modeling studies, accompanied by melting experiments of relevant materials, would also help to enhance the scientific return from the remote sensing data sets.

[36] **Acknowledgments.** The authors thank Denton Ebel and an anonymous reviewer for constructive reviews of an earlier version of this

paper. We thank the MESSENGER team for the development, cruise, orbit insertion, and orbital operations of the MESSENGER spacecraft. This work is supported by the NASA Discovery Program under contract NAS5–97271 to The Johns Hopkins University Applied Physics Laboratory and NASW-00002 to the Carnegie Institution of Washington. S.Z.W. thanks Frances E. Jenner for helpful discussions during manuscript preparation.

References

Adler, I., et al. (1973), Apollo 15 and 16 results of the integrated geochemical instrument, *Moon*, *7*, 487–504, doi:10.1007/BF00564649.

Anders, E. (1977), Chemical compositions of the Moon, Earth, and eucrite parent body, *Philos. Trans. R. Soc. London, Ser. A*, *285*, 23–40, doi:10.1098/rsta.1977.0040.

Asimov, P. D., and M. S. Ghiorso (1998), Algorithmic modifications extending MELTS to calculate subsolidus phase relations, *Am. Mineral.*, *83*, 1127–1131.

Becker, K. J., L. A. Weller, K. L. Edmundson, T. L. Becker, M. S. Robinson, A. C. Enns, and S. C. Solomon (2012), Global controlled mosaic of Mercury from MESSENGER orbital images, *Lunar Planet. Sci.*, *43*, abstract 2654.

Benedix, G. K., D. S. Lauretta, and T. J. McCoy (2005), Thermodynamic constraints on the formation conditions of winonaites and silicate-bearing IAB irons, *Geochim. Cosmochim. Acta*, *69*, 5123–5131, doi:10.1016/j.gca.2005.03.048.

Blewett, D. T., B. R. Hawke, and P. G. Lucey (2002), Lunar pure anorthosite as a spectral analog for Mercury, *Meteorit. Planet. Sci.*, *37*, 1245–1254, doi:10.1111/j.1945-5100.2002.tb00893.x.

Bouwer, S. D. (1983), Intermediate-term epochs in solar soft X ray emission, *J. Geophys. Res.*, *88*, 7823–7830, doi:10.1029/JA088iA10p07823.

Brearley, A. J., and R. H. Jones (1998), Chondritic meteorites, in *Planetary Materials*, *Rev. Mineral.*, vol. 36, edited by J. J. Papike, pp. 3.1–3.398, Mineral. Soc. Am., Washington, D. C.

Burbine, T. H., T. J. McCoy, L. R. Nittler, G. K. Benedix, E. A. Cloutis, and T. L. Dickinson (2002), Spectra of extremely reduced assemblages: Implications for Mercury, *Meteorit. Planet. Sci.*, *37*, 1233–1244, doi:10.1111/j.1945-5100.2002.tb00892.x.

Buseck, P. R., and E. F. Holdsworth (1972), Mineralogy and petrology of the Yilmia enstatite chondrite, *Meteoritics*, *7*, 429–448, doi:10.1111/j.1945-5100.1972.tb00124.x.

Clark, P. E., and J. I. Trombka (1997), Remote X-ray spectrometry for NEAR and future missions: Modeling and analyzing X-ray production from source to surface, *J. Geophys. Res.*, *102*, 16,361–16,384, doi:10.1029/97JE01086.

Clayton, R. N., T. K. Mayeda, and A. E. Rubin (1984), Oxygen isotopic compositions of enstatite chondrites and aubrites, *Proc. Lunar Planet. Sci. Conf. 15th*, Part I, *J. Geophys. Res.*, *88*, suppl., C245–C249, doi:10.1029/JB089iS01p0C245.

Crosby, N. B., M. J. Aschwanden, and B. R. Dennis (1993), Frequency distributions and correlations of solar X-ray flare parameters, *Sol. Phys.*, *143*, 275–299, doi:10.1007/BF00646488.

Denevi, B. W., et al. (2009), The evolution of Mercury's crust: A global perspective from MESSENGER, *Science*, *324*, 613–618.

Denevi, B. W., M. S. Robinson, S. L. Murchie, C. M. Ernst, P. K. Byrne, S. C. Solomon, and P. N. Peplowski (2012), The distribution of young plains on Mercury, *EPSC Abstr.*, *7*, EPSC2012-812.

Dere, K. P., E. Landi, H. E. Mason, B. C. Monsignori Fossi, and P. R. Young (1997), CHIANTI: An atomic database for emission lines, *Astron. Astrophys. Suppl. Ser.*, *125*, 149–173, doi:10.1051/aas:1997368.

Donnelly, R. F. (1976), Empirical models of solar flare X ray and EUV emission for use in studying their E and F region effects, *J. Geophys. Res.*, *81*, 4745–4753, doi:10.1029/JA081i025p04745.

Ebel, D. S. (2006), Condensation of rocky material in astrophysical environments, in *Meteorites and the Early Solar System II*, edited by D. Lauretta, H. Y. McSween Jr., and R. P. Binzel, pp. 253–277, Univ. of Arizona Press, Tucson, Ariz.

Ebel, D. S., and C. M. O'D. Alexander (2011), Equilibrium condensation from chondritic porous IDP enriched vapor: Implications for Mercury and enstatite chondrite origins, *Planet. Space Sci.*, *59*, 1888–1894, doi:10.1016/j.pss.2011.07.017.

El Goresy, A., H. Yabuki, K. Ehlers, D. Woolum, and E. Pernicka (1988), Qingzhen and Yamato-691: A tentative alphabet for the EH chondrites, *Proc. NIPR Symp. Antarct. Meteorit.*, *1*, 65–101.

Evans, L. G., et al. (2012), Major-element abundances on the surface of Mercury: Results from the MESSENGER Gamma-Ray spectrometer, *J. Geophys. Res.*, doi:10.1029/2012JE004178, in press.

Fassett, C. I., J. W. Head, D. T. Blewett, C. R. Chapman, J. L. Dickson, S. L. Murchie, S. C. Solomon, and T. R. Watters (2009), Caloris impact basin: Exterior geomorphology, stratigraphy, morphometry, radial sculpture, and smooth plains deposits, *Earth Planet. Sci. Lett.*, *285*, 297–308, doi:10.1016/j.epsl.2009.05.022.

Fludra, A., and J. T. Schmelz (1999), The absolute coronal abundances of sulfur, calcium, and iron from Yohkoh-BCS flare spectra, *Astron. Astrophys.*, *348*, 286–294.

Foley, C. N., L. R. Nittler, T. J. McCoy, L. F. Lim, M. R. M. Brown, R. D. Starr, and J. I. Trombka (2006), Minor element evidence that Asteroid 433 Eros is a space-weathered ordinary chondrite parent body, *Icarus*, *184*, 338–343, doi:10.1016/j.icarus.2006.05.011.

Fraser, G. W., et al. (2010), The Mercury Imaging X-ray Spectrometer (MIXS) on BepiColombo, *Planet. Space Sci.*, *58*, 79–95, doi:10.1016/j.pss.2009.05.004.

Garcia, H. A. (1994), Temperature and emission measure from GOES soft X-ray measurements, *Sol. Phys.*, *154*, 275–308, doi:10.1007/BF00681100.

Ghiorso, M. S., and R. O. Sack (1995), Chemical mass transfer in magmatic process. IV. A revised and internally consistent thermodynamic model for the interpolation and extrapolation of liquid-solid equilibria in magmatic systems at elevated temperatures and pressures, *Contrib. Mineral. Petrol.*, *119*, 197–212, doi:10.1007/BF00307281.

Grande, M., et al. (2007), The D-CIXS X-ray spectrometer on the SMART-1 mission to the Moon–First results, *Planet. Space Sci.*, *55*, 494–502, doi:10.1016/j.pss.2006.08.004.

Head, J. W., et al. (2008), Volcanism on Mercury: Evidence from the first MESSENGER flyby, *Science*, *321*, 69–72, doi:10.1126/science.1159256.

Head, J. W., et al. (2011), Flood volcanism in the northern high latitudes of Mercury revealed by MESSENGER, *Science*, *333*, 1853–1856, doi:10.1126/science.1211997.

Ho, G. C., R. D. Starr, R. E. Gold, S. M. Krimigis, J. A. Slavin, D. N. Baker, B. J. Anderson, R. L. McNutt Jr., L. R. Nittler, and S. C. Solomon (2011), Observations of suprathermal electrons in Mercury's magnetosphere during the three MESSENGER flybys, *Planet. Space Sci.*, *59*, 2016–2025, doi:10.1016/j.pss.2011.01.011.

Ho, G. C., S. M. Krimigis, R. E. Gold, D. N. Baker, B. J. Anderson, H. Korth, J. A. Slavin, R. L. McNutt, and S. C. Solomon (2012), Spatial distribution and spectral characteristics of energetic electrons in Mercury's magnetosphere, *J. Geophys. Res.*, *117*, A00M04, doi:10.1029/2012JA017983.

Jenner, F. E., and H. S. C. O'Neill (2012), Analysis of 60 elements in 616 ocean floor basaltic glasses, *Geochem. Geophys. Geosyst.*, *13*, Q02005, doi:10.1029/2011GC004009.

Keil, K. (1968), Mineralogical and chemical relationships among enstatite chondrites, *J. Geophys. Res.*, *73*, 6945–6976, doi:10.1029/JB073i022p06945.

Killen, R. M., A. E. Potter, P. Reiff, M. Sarantos, B. V. Jackson, P. Hick, and B. Giles (2001), Evidence for space weather at Mercury, *J. Geophys. Res.*, *106*, 20,509–20,526, doi:10.1029/2000JE001401.

Killen, R. M., M. Sarantos, A. E. Potter, and P. H. Reiff (2004), Source rates and ion recycling rates for Na and K in Mercury's atmosphere, *Icarus*, *171*, 1–19, doi:10.1016/j.icarus.2004.04.007.

Kurat, G., E. Zinner, and F. Branstätter (1992), An ion microprobe study of a unique oldhamite-pyroxenite fragment from the Bustee aubrite, *Meteoritics*, *27*, 246–247.

Leitch, C. A., and J. V. Smith (1982), Petrography, mineral chemistry and origin of Type 1 enstatite chondrites, *Geochim. Cosmochim. Acta*, *46*, 2083–2097, doi:10.1016/0016-7037(82)90187-9.

Lim, L. F., and L. R. Nittler (2009), Elemental composition of 433 Eros: New calibration of the NEAR-Shoemaker XRS data, *Icarus*, *200*, 129–146, doi:10.1016/j.icarus.2008.09.018.

Mason, B. (1966), The enstatite chondrites, *Geochim. Cosmochim. Acta*, *30*, 23–39, doi:10.1016/0016-7037(66)90089-5.

McClintock, W. E., et al. (2008), Spectroscopic observations of Mercury's surface reflectance during MESSENGER's first Mercury flyby, *Science*, *321*, 62–65, doi:10.1126/science.1159933.

McClintock, W. E., R. J. Vervack Jr., E. T. Bradley, R. M. Killen, N. Mouawad, A. L. Sprague, M. H. Burger, S. C. Solomon, and N. R. Izenberg (2009), MESSENGER observations of Mercury's exosphere: Detection of magnesium and distribution of constituents, *Science*, *324*, 610–613.

McCoy, T. J. (1998), A pyroxene-oldhamite clast in Bustee: Igneous aubritic oldhamite and a mechanism for the Ti enrichment in aubritic troilite, *Antarct. Meteorite Res.*, *11*, 34–50.

McCoy, T. J., T. L. Dickinson, and G. E. Lofgren (1999), Partial melting of the Indarch (EH4) meteorite: A textural, chemical, and phase relations view of melting and melt migration, *Meteorit. Planet. Sci.*, *34*, 735–746, doi:10.1111/j.1945-5100.1999.tb01386.x.

McCubbin, F. M., M. A. Riner, K. E. Vander Kaaden, and L. K. Burkemper (2012), Is Mercury a volatile-rich planet?, *Geophys. Res. Lett.*, *39*, L09202, doi:10.1029/2012GL051711.

Mittlefehldt, D. W., T. J. McCoy, C. A. Goodrich, and A. Kracher (1998), Non-chondritic meteorites from asteroidal bodies, in *Planetary Materials*, *Rev. Mineral.*, vol. 36, edited by J. J. Papike, pp. 4.1–4.195, Mineral. Soc. of Am., Washington, D. C.

Mura, A., P. Wurz, H. I. M. Lichtenegger, H. Schleicher, H. Lammer, D. Delcourt, A. Milillo, S. Orsini, S. Massetti, and M. L. Khodachenko (2009), The sodium exosphere of Mercury: Comparison between observations during Mercury's transit and model results, *Icarus*, *200*, 1–11, doi:10.1016/j.icarus.2008.11.014.

Murchie, S. L., et al. (2008), Geology of the Caloris basin, Mercury: A view from MESSENGER, *Science*, *321*, 73–76, doi:10.1126/science.1159261.

Narendranath, S., et al. (2011), Lunar X-ray fluorescence observations by the Chandrayaan-1 X-ray Spectrometer (C1XS): Results from the nearside southern highlands, *Icarus*, *214*, 53–66, doi:10.1016/j.icarus.2011.04.010.

Nittler, L. R., et al. (2001), X-ray fluorescence measurements of the surface elemental composition of asteroid 433 Eros, *Meteorit. Planet. Sci.*, *36*, 1673–1695, doi:10.1111/j.1945-5100.2001.tb01856.x.

Nittler, L. R., et al. (2011), The major-element composition of Mercury's surface from MESSENGER X-ray spectrometry, *Science*, *333*, 1847–1850, doi:10.1126/science.1211567.

Okada, T., M. Kato, Y. Yamashita, K. Shirai, Y. Yamamoto, T. Matsuda, H. Tsunemi, and S. Kitamoto (2002), Lunar X-ray spectrometer experiment on the SELENE mission, *Adv. Space Res.*, *30*, 1909–1914, doi:10.1016/S0273-1177(02)00487-8.

Okada, T., K. Shirai, Y. Yamamoto, T. Arai, K. Ogawa, K. Hosono, and M. Kato (2006), X-ray fluorescence spectrometry of asteroid Itokawa by Hayabusa, *Science*, *312*, 1338–1341, doi:10.1126/science.1125731.

Palme, H., and H. Beer (1993), Abundances of the elements in the solar system, in *Instruments, Methods, Solar System*, *Landolt-Börstein: Astron. and Astrophys.*, vol. 3a, edited by H. H. Voigt, pp. 196–221, Springer, Berlin.

Palme, H., and A. Jones (2003), Solar system abundances of the elements, in *Treatise on Geochemistry*, vol. 1, *Meteorites, Comets, and Planets*, edited by A. M. Davis, pp. 41–61, Elsevier, Amsterdam.

Palme, H., and H. S. C. O'Neill (2003), Cosmochemical estimates of mantle composition, in *Treatise on Geochemistry*, vol. 2, *The Mantle and Core*, edited by R. W. Carlson, pp. 1–38, Elsevier, Amsterdam.

Peplowski, P. N., et al. (2011), Radioactive elements on Mercury's surface from MESSENGER: Implications for the planet's formation and evolution, *Science*, *333*, 1850–1852, doi:10.1126/science.1211576.

Peplowski, P. N., D. J. Lawrence, E. A. Rhodes, A. L. Sprague, B. W. Denevi, L. G. Evans, J. W. Head, and S. C. Solomon (2012), Variations in the abundances of potassium and thorium on the surface of Mercury: Results from the MESSENGER Gamma-Ray Spectrometer, *J. Geophys. Res.*, doi:10.1029/2012JE004141, in press.

Robinson, M. S., and P. G. Lucey (1997), Recalibrated Mariner 10 color mosaics: Implications for Mercurian volcanism, *Science*, *275*, 197–200, doi:10.1126/science.275.5297.197.

Rubin, A. E. (1983), Impact melt-rock clasts in the Hvittis enstatite chondrite breccia: Implications for a genetic relationship between EL chondrites and aubrites, *Proc. Lunar Planet. Sci. Conf. 14th*, Part I, suppl., *J. Geophys. Res.*, *88*, B293– B300, doi:10.1029/JB088iS01p0B293.

Schlemm, C. E., II, et al. (2007), The X-Ray Spectrometer on the MESSENGER spacecraft, *Space Sci. Rev.*, *131*, 393–415, doi:10.1007/s11214-007-9248-5.

Sprague, A. L., D. M. Hunten, and K. Lodders (1995), Sulfur at Mercury, elemental at the poles and sulfides in the regolith, *Icarus*, *118*, 211–215, doi:10.1006/icar.1995.1186.

Sprague, A. L., J. P. Emery, K. L. Donaldson, R. W. Russell, D. K. Lynch, and A. L. Mazuk (2002), Mercury: Mid-infrared (3–13.5 μm) observations show heterogeneous composition, presence of intermediate and basic soil types, and pyroxene, *Meteorit. Planet. Sci.*, *37*, 1255–1268, doi:10.1111/j.1945-5100.2002.tb00894.x.

Spudis, P. D., and J. E. Guest (1988), Stratigraphy and geologic history of Mercury, in *Mercury*, edited by F. Vilas, C. R. Chapman, and M. S. Matthews, pp. 118–164, Univ. of Arizona Press, Tucson, Ariz.

Starr, R., et al. (2000), Instrument calibrations and data analysis procedures for the NEAR X-Ray Spectrometer, *Icarus*, *147*, 498–519, doi:10.1006/icar.2000.6453.

Starr, R. D., D. Schriver, L. R. Nittler, S. Z. Weider, P. K. Byrne, G. C. Ho, E. A. Rhodes, C. E. Schlemm II, S. C. Solomon, and P. M. Trávníček (2012), MESSENGER detection of electron-induced X-ray fluorescence from Mercury's surface, *J. Geophys. Res.*, *117*, E00L02, doi:10.1029/2012JE004118.

Strom, R. G., and G. Neukum (1988), The cratering record on Mercury and the origin of impacting objects, in *Mercury*, edited by F. Vilas, C. R. Chapman, and M. S. Matthews, pp. 336–373, Univ. of Arizona Press, Tucson, Ariz.

Strom, R. G., C. R. Chapman, W. J. Merline, S. C. Solomon, and J. W. Head III (2008), Mercury cratering record viewed from MESSENGER's first flyby, *Science*, *321*, 79–81, doi:10.1126/science.1159317.

Swinyard, B. M., et al. (2009), X-ray fluorescence of the Moon by SMART-1/D-CIXS and the first detection of Ti K_α from the lunar surface, *Planet. Space Sci.*, *57*, 744–750, doi:10.1016/j.pss.2009.01.009.

Taylor, S. R. (1982), *Planetary Science: A Lunar Perspective*, 502 pp., Lunar and Planet. Inst., Houston, Tex.

Trask, N. J., and J. E. Guest (1975), Preliminary geologic terrain map of Mercury, *J. Geophys. Res.*, *80*, 2461–2477, doi:10.1029/JB080i017p02461.

Trombka, J. I., et al. (2000), The elemental composition of asteroid 433 Eros: Results of the NEAR-Shoemaker X-ray Spectrometer, *Science*, *289*, 2101–2105, doi:10.1126/science.289.5487.2101.

Vervack, R. J., Jr., W. E. McClintock, R. M. Killen, A. L. Sprague, B. J. Anderson, M. H. Burger, E. T. Bradley, N. Mouawad, S. C. Solomon, and N. R. Izenberg (2010), Mercury's complex exosphere: Results from MESSENGER's third flyby, *Science*, *329*, 672–675, doi:10.1126/science.1188572.

Vilas, F. (1988), Surface composition of Mercury from reflectance spectrophotometry, in *Mercury*, edited by F. Vilas, C. R. Chapman, and M. S. Matthews, pp. 59–76, Univ. of Arizona Press, Tucson, Ariz.

Watters, T. R., and M. Prinz (1979), Aubrites: Their origin and relationship to chondrites, *Proc. Lunar Planet. Sci. Conf.*, *10th*, 1073–1093.

Weider, S. Z., et al. (2012), The Chandrayaan-1 X-ray Spectrometer: First results, *Planet. Space Sci.*, *60*, 217–228, doi:10.1016/j.pss.2011.08.014.

Wheelock, M. M., K. Keil, C. Floss, G. J. Taylor, and G. Crozaz (1994), REE geochemistry of oldhamite-dominated clasts from the Norton County aubrite: Igneous origin of oldhamite, *Geochim. Cosmochim. Acta*, *58*, 449–458, doi:10.1016/0016-7037(94)90476-6.

Zuber, M. T., et al. (2012), Topography of the northern hemisphere of Mercury from MESSENGER laser altimetry, *Science*, *336*, 217–220, doi:10.1126/science.1218805.

Zurbuchen, T. H., et al. (2011), MESSENGER observations of the spatial distribution of planetary ions near Mercury, *Science*, *333*, 1862–1865, doi:10.1126/science.1211302.